Geophysical Journal International

Geophys. J. Int. (2021) **226,** 1730–1746
Advance Access publication 2021 May 07
GJI Geodynamics and Tectonics

doi: https://doi.org/10.1093/gji/ggab185

Multiscale, radially anisotropic shear wave imaging of the mantle underneath the contiguous United States through joint inversion of USArray and global data sets

Robert W. Porritt,[1] Thorsten W. Becker,[1,2] Lapo Boschi[3,4,5] and Ludwig Auer[6]

[1] *Institute for Geophysics, Jackson School of Geosciences, The University of Texas at Austin, 2305 Speedway Stop, C1160 Austin, TX 78712-1692, USA. E-mail: rwporritt@gmail.com*
[2] *Department of Geosciences, Jackson School of Geosciences, The University of Texas at Austin, Austin, TX 78712, USA*
[3] *Dipartimento di Geoscienze, Università degli Studi di Padova, 35131 Padova PD, Italy*
[4] *Institut des Sciences de la Terre de Paris, Sorbonne Université, CNRS-INSU, ISTeP UMR 7193, Paris, France*
[5] *Istituto Nazionale di Geofisica e Vulcanologia, Bologna, Via Donato Creti, 12, 40128 Bologna, Italy*
[6] *Swiss Seismological Survey, ETH Zurich, Zurich, Switzerland*

Accepted 2021 May 5. Received 2021 April 26; in original form 2020 October 8

SUMMARY

EarthScope's USArray seismic component provided unprecedented coverage of the contiguous United States and has therefore spurred significant advances in tomographic imaging and geodynamic modelling. Here, we present a new global, radially anisotropic shear wave velocity tomography model to investigate upper mantle structure and North American Plate dynamics, with a focus on the contiguous United States. The model uses a data-adaptive mesh and traveltimes of both surface waves and body waves to constrain structure in the crust and mantle in order to arrive at a more consistent representation of the subsurface compared to what is provided by existing models. The resulting model is broadly consistent with previous global models at the largest scales, but there are substantial differences under the contiguous United States where we can achieve higher resolution. On these regional scales, the new model contains short wavelength anomalies consistent with regional models derived from USArray data alone. We use the model to explore the geometry of the subducting Farallon Slab, the presence of upper mantle high velocity anomalies, low velocity zones in the central and eastern United States and evaluate models of dynamic topography in the Cordillera. Our models indicate a single, shallowly dipping, discontinuous slab associated with the Farallon Plate, but there are remaining imaging challenges. Inferring dynamic topography from the new model captures both the long-wavelength anomalies common in global models and the short-wavelength anomalies apparent in regional models. Our model thus bridges the gap between high-resolution regional models within the proper uppermost mantle context provided by global models, which is crucial for understanding many of the fundamental questions in continental dynamics.

Key words: Structure of the Earth; Joint inversion; Tomography; Body waves; Seismic tomography; Surface waves and free oscillations.

1 INTRODUCTION

EarthScope's USArray is a paradigm shifting seismic experiment which blanketed the contiguous United States and Alaska with evenly spaced broadband seismometers (Fig. 1). The high station density with ∼70–85 km interstation spacing and best practice installations has yielded several terabytes of high-quality seismic waveform data. This has facilitated a new generation of tomographic models seeking to better understand the geological processes which shaped North America. While the regional patterns between models of the same type (e.g. body waves only) are highly similar (e.g. Becker 2012; Pavlis *et al.* 2012), there are significant differences between larger-scale models depending on the data sets and methodologies used in their development (e.g. Schmandt & Lin 2014; Clouzet *et al.* 2018; Golos *et al.* 2018). Reconciling these differences could provide valuable further insights into the geological history of North America. In particular, studies of the links between mantle convection and surface deformation require a consistent imaging of asthenospheric anomalies as well as lithospheric structure and thickness accounting for radial anisotropy (e.g. Yuan & Romanowicz 2010). We derive and interpret a new tomographic model which includes USArray data and uses multiscale resolution

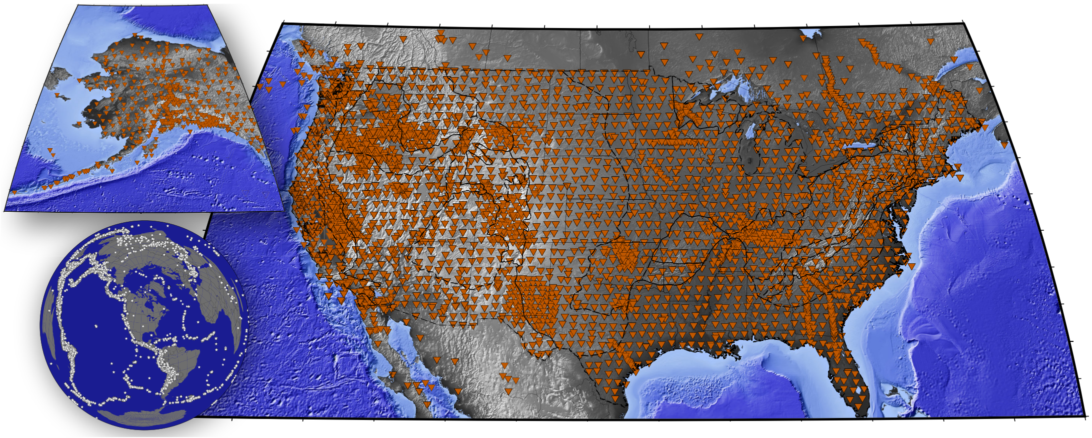

Figure 1. Location map of stations in the contiguous United States and Alaska (upper inset). Lower inset depicts event coverage centred on the contiguous United States.

to smoothly resolve both the densely sampled USArray footprint and global structure (*cf.* Bijwaard *et al.* 1998). We adopt a simple, ray-theoretical model of wave propagation and implement inversion methods from a publicly available library for high-performance computing (Auer *et al.* 2014).

The contiguous United States has a first-order, west–east structural contrast where the high topography of the tectonically active western United States contrasts sharply with the low topography east of the Rocky Mountains within the older part of the lithosphere. Corresponding differences at depth are consistently imaged in tomographic models as relatively low or high seismic velocity upper mantle in the west and east, respectively, and interpreted as lithospheric thickness variations (e.g. Yuan & Romanowicz 2010; Schaeffer & Lebedev 2014). Mid to lower mantle high velocity anomalies underneath North America reflect a long history of subduction off the United States west coast (e.g. Grand *et al.* 1997; van der Lee & Frederiksen 2005; Bedle & van der Lee 2009; Simmons *et al.* 2010; Sigloch 2011).

There have been significant advances in our understanding of these features through the utilization of USArray. For example, several body wave tomography studies (e.g. Xue & Allen 2007; Burdick *et al.* 2008, 2017; Obrebski *et al.* 2010, 2011; Schmandt & Humphreys 2010; James *et al.* 2011; Porritt *et al.* 2014; Schmandt & Lin 2014*;* Boyce *et al.* 2019; Hawley & Allen 2019) have shown evidence of high velocity slabs and delaminated lithosphere in the upper mantle and transition zone. Of these, the studies which span the contiguous United States also show the existence of a handful of low velocity features in the upper mantle along the east coast, for example, which are corroborated by surface wave tomographic models (e.g. Wagner *et al.* 2018). Below the Mantle Transition Zone (MTZ), several isolated, large volume, high velocity anomalies are imaged. These are suggestive of a complex subduction history of the Farallon Slab (FS) system (e.g. Bunge & Grand 2000*;* van der Lee *et al.* 2008; Liu & Stegman 2012) and recent re-interpretations by Sigloch & Mihalynuk (2013) and Clennett *et al.* (2020) suggest they may reflect several distinct episodes of collision along the west coast rather than a single system.

Global tomographic models constrain long-wavelength Earth structure, for example uppermost mantle continental and oceanic plate structure, slabs in the mid to lower mantle and two, large low shear velocity provinces near the core–mantle boundary (e.g. Becker & Boschi 2002). However, these models are typically limited in resolution due to computational challenges of generating high-frequency synthetic seismograms for waveform-based methods, merging different types of data sets, as well as challenges due to the uneven distribution of seismic sources and receivers around the globe. Variable resolution, global *P*-wave tomography models have long been used (e.g. Bijwaard *et al.* 1998; Li *et al.* 2008; Burdick *et al.* 2017), but only few variable resolution, joint surface and body wave tomographic *S*-wave models exist (e.g. Auer *et al.* 2014). In addition to providing complementary petrological and thermal constraints to *P*-wave models, *S*-wave models can more readily use surface wave measurements which are important for the uppermost mantle and constraining radial anisotropy.

Regional tomographic models can typically achieve higher resolution than global models due to their lower computational cost, but often require simplifying assumptions which may make their results incompatible with global models. For instance, relative traveltime based models sacrifice absolute arrival times relative to a global background model in exchange for higher fidelity, cross-correlated measurements (VanDecar & Crosson 1990). This requires station and event correction factors to be added to absorb traveltime perturbations along the ray path which are not modeled directly. Therefore, the wave speed perturbations recovered in regional models are internally consistent but cannot be directly interpreted as absolute seismic velocities, making their integration into a global dynamic model a non-trivial problem (e.g. Ghosh *et al.* 2013; Wang & Becker 2019).

Resolution issues aside, previous regional tomographic models have driven a range of geodynamic interpretations and modelling. For example, Liu & Stegman (2012) focus on subducting slab geometry underneath the western United States to propose a model of slab-tear induced upwelling related volcanisms. The distributed and segmented appearance of slab anomalies (e.g. Schmandt & Humphreys 2010) raises a number of other related questions such as the nature of vertical mass transport in actively deforming regions (e.g. Burkett & Gurnis 2013; Zhou *et al.* 2018), and the role of lithospheric delamination (e.g. Boyd *et al.* 2004; West *et al.* 2009; Levander *et al.* 2011). Dynamic topography and intriguing uplift patterns as driven by presumably hot, rising mantle anomalies within the western United States suggest asthenospheric flow as the cause of crustal deformation (e.g. Ghosh *et al.* 2013; Liu 2015; Becker *et al.* 2015). Yet, the degree to which uppermost mantle anomalies are imaged as connected or detached in tomographic models, for example, still depends at least partially on model data selection even for USArray based models. If a tomography model primarily uses body wave data, for example, results may be skewed by near vertical smearing along ray paths in the shallow mantle. Alternatively, surface-wave-derived models tend to smooth structures laterally and have limited sensitivity to the mid to lower mantle (e.g. Porritt *et al.* 2014; Moulik & Ekstrom 2014; Golos *et al.* 2018). To explore these trade-offs, and to avoid having to merge models with different scope and resolution length-scales, we here present a new tomographic model, which is global in scope, but data adaptive to leverage the USArray, and which combines both body wave and surface wave observations.

2 DATA AND METHODS

Our tomographic imaging approach follows Auer *et al.* (2014). This method utilizes traveltime observations relative to a 1-D reference model, PREM (Dziewonski & Anderson 1981) and a ray theory approximation (e.g. Woodhouse 1981; Boschi & Ekström 2002) to invert for both horizontally and vertically polarized shear velocity perturbations (dV_{sh} and dV_{sv}, respectively), that is allowing for radial anisotropy while allowing teleseismic *S* phases and frequency dependent surface wave measurements to be inverted jointly for shear velocity. The model is parametrized on a global, data adaptive mesh such that high resolution is achieved in areas of high ray density (*cf.* Bijwaard *et al.* 1998). The inversion itself is implemented through the PETSc library to allow efficient computations (Balay *et al.* 2020).

Our data set is an expansion of that of Auer *et al.* (2014). In that study, the authors chose to focus on several S, SS, SSS, SKS, SKKS, ScS, sScS, ScS2, ScS3 and ScS4 (i.e. S+) phases from Ritsema *et al.* (2011) for the body wave constraints, and on Rayleigh and Love wave dispersion measurements, corrected for azimuthal anisotropy, from Ekström (2011) and Visser *et al.* (2008). Our new model adds to these data sets S and SKS traveltimes measured by analysts at the Array Network Facility (ANF) [anf.ucsd.edu/tools/events] and S, SS, SSS, ScS and ScSScS traveltimes measured by Lai *et al.* (2019) using an adaptive empirical wavelet construction (Tables 1, S1). These data sets total an additional 442 646 S + body wave measurements after summary ray construction. The data of Lai *et al.* (2019) includes a global distribution of stations, while the ANF only uses stations of the USArray giving the new model improved data coverage both globally and within the United States. Body wave delay times are adjusted to a nominal 35-km-thick crust assuming variations in crustal thickness based on Crust1.0 (Laske *et al.* 2013), 3.5 km s^{-1} crustal shear velocity and 4.5 km s^{-1} uppermost mantle shear velocity. Additionally, ambient noise Rayleigh and Love wave measurements from Ekström (2014) are included to better constrain the shallow portion of the model. This Rayleigh and Love wave data set includes measurements from 15 to 40 s period and 421 793 and 274 468 delay times, respectively. Other publicly available data sets, including the International Seismological Centre Engdahl-van der Hilst-Buland (EHB) body wave arrival time catalog (Weston *et al.* 2018; Engdahl *et al.* 1998, 2020; International Seismological Centre 2020) and the Automated Surface Wave Measuring System (Jin & Gaherty 2015), were considered, but not included in the final model to avoid inconsistencies due to different body wave measurement approaches (e.g. Lai *et al.* 2019) and to reduce data redundancy, particularly for the weighting between dV_{sv} and dV_{sh} sensitivity and between body wave and surface wave constraints.

The sensitivity to slowness matrices for each data set are calculated using the infinite frequency (ray theory) approximation. Body waves which include a core leg (e.g. SKS, SKKS) have high sensitivity to dV_{sv}, whereas other body wave phases are more sensitive to dV_{sh}. The surface wave sensitivity kernels to velocity at depth for each lateral gridpoint are based on a reference model that combines Crust1.0 (Laske *et al.* 2013) and PREM (Dziewonski & Anderson 1981). The initial matrices use a parametrization with 34 layers, more densely sampled in the crust than the mantle and globally mesh the Earth into voxels 0.3125° × 0.3125° (Fig. S1). Inverting this matrix directly for two shear velocity parameters, dV_{sv} and dV_{sh}, would require solving for 4.5×10^7 model parameters. Considering the available data set is also on the order of 10^7 and the need for extra space in the matrix for regularization, inversion of this matrix quickly grows into a difficult computational problem. Therefore, the matrices are projected onto an adaptive mesh, which merges neighboring voxels when their hit counts are below a threshold value (Auer *et al.* 2014), up to a maximum coarseness of 5° × 5°. The threshold values were arrived at through trial and error to balance having as fine of a mesh as possible in the contiguous United States and Alaska while smoothly transitioning to the rest of the globe and reducing the total number of model elements to $\sim 9.5 \times 10^5$ parameters (Figs 2 and 3). This represents a 10-fold increase in degrees of freedom, compared to the modelling performed in Auer *et al.* (2014).

The matrix inversion utilizes the PETSc toolkit (github.com/auerl; mcs.anl.gov/petsc; Balay *et al.* 2020). As in Auer *et al.* (2014), we impose damping on the model roughness, norm and difference between the dV_{sh} and dV_{sv} results (i.e. damping towards isotropy). The weights of these regularization equations were tested to evaluate the trade-off between data fit, smoothness and leakage between the isotropic and anisotropic components (Figs S2 and S3). As in Auer *et al.* (2014), the vertical roughness damping in the crust and upper mantle is doubled compared with the lateral damping and this weight is linearly increased to 5-fold below the mantle transition zone. Similarly, the anisotropic difference damping is linearly scaled from the global value to 10-fold below the transition zone (*cf.* Kustowksi *et al.* 2008). To account for the variable mesh, a function is applied to the roughness damping to reduce the damping at the finest grid scale relative to the coarsest grid by a factor of four. Finally, to account for residual uncertainties in the near-surface velocity at individual stations and potential errors in the event timing and location, station and event corrections are added to the model vector.

The weights of these damping parameters can have significant and interacting effects on the final model. We found trade-off between model variance and data fit for roughness damping to have the most significant effect with a relatively clear bow in the L curve (Fig. S2). On the other hand, norm damping had little effect on the data fit and rather worked to adjust the peak-to-peak amplitude in the final model, as expected. The difference damping is designed to control the leakage between the isotropic structure and the anisotropic structure, but the trade-off test does not show an optimum value because of cross-talk between isotropic and anisotropic structure (Fig. S3). We chose a preferred value that returns similar amplitudes in radial anisotropy as in SAVANI.

3 RESOLUTION

Checkerboard tests are an imperfect but nonetheless helpful tool to visualize the spatial scale of resolvable features and the smearing that can be expected due to data coverage. In Figs 2 and 3,

Table 1. Summary of new data sets used in the inversion of SAVANI-US. For the full data listing (see Table S1).

Origin	Phase	Surface wave mode	Surface wave period	Number	Sensitivity	Weight	Station distribution
Array Network Facility (ANF)	S	N/A	N/A	220 313	dV_{sh}	15	Contiguous US + Alaska
	SKS	N/A	N/A	12 174	dV_{sv}	9	Contiguous US + Alaska
Lai *et al.* (2019)	ScS	N/A	N/A	23 301	dV_{sh}	3	Global
	ScSScS	N/A	N/A	10 274	dV_{sh}	3	Global
	S	N/A	N/A	129 895	dV_{sh}	15	Global
	SS	N/A	N/A	53 127	dV_{sh}	3	Global
	SSS	N/A	N/A	11 836	dV_{sh}	3	Global
Ekstrom (2014, 2017)	Rayleigh	Fundamental	15	34 504	dV_{sv}	2	Contiguous US
			20	47 620	dV_{sv}	2	Contiguous US
			25	70 914	dV_{sv}	2	Contiguous US
			30	97 199	dV_{sv}	2	Contiguous US
			35	90 712	dV_{sv}	2	Contiguous US
			40	80 844	dV_{sv}	2	Contiguous US
	Love	Fundamental	15	33 233	dV_{sh}	3	Contiguous US
			20	38 407	dV_{sh}	3	Contiguous US
			25	50 239	dV_{sh}	3	Contiguous US
			30	58 955	dV_{sh}	3	Contiguous US
			35	51 474	dV_{sh}	3	Contiguous US
			40	42 160	dV_{sh}	3	Contiguous US

we present checkerboard tests at the global and regional scales, respectively, for a variety of depths and checker sizes. These figures compare the resolution with and without the new data relative to Auer *et al.* (2014), inverted on the same mesh with the same regularization parameters. Within the crust, at 15 km depth, resolution is poor outside the contiguous United States, but the new model has resolution at the ∼2.5° × 2.5° scale within the contiguous United States due to the ambient noise measurements from Ekström (2014, 2017). At lithospheric depths, ∼60–250 km, we can see substantial improvement with the new data, particularly in the central and eastern United States. This is primarily due to the ANF data, which contains significant station coverage that was not available previously. This pattern is seen throughout the mid to lower mantle, but the differences are less significant than at lithospheric depths. This reflects the ray turning depth of direct S phases which comprise the majority of our measurements, the coarsening of the mesh below ∼1300 km, and the relatively few SKS and ScS phases added from the ANF and Lai *et al.* (2019) data, respectively. Overall, our new model's resolution approaches the resolvable length scale obtained by regionally focused models in the contiguous United States, but resolution at the global scale is somewhat reduced due to the coarse mesh outside the contiguous United States and in the deeper mantle.

4 GLOBAL SCALE RESULTS

Our new model, SAVANI-US, contains several first order features which are consistent with earlier models at the global scale (Table 2; Fig. 4). This is most clearly seen in the upper 200 km where the long wavelength features of high velocity cratonic lithosphere contrasts with low velocity regions of active deformation (e.g. oceanic spreading centres and diffuse boundaries). At 45 km depth, there are some slight differences seen in SAVANI (Auer *et al.* 2014), S40RTS (Ritsema *et al.* 2011), S362ANI + M (Moulik & Ekström 2014) and SAVANI-US. SAVANI has a notably higher velocity lithosphere than the other models and S40RTS has lower overall positive and negative amplitudes. These differences may be due to differences in crustal corrections, regularization choices and are at the shallow limit of what these models can resolve without high-density station coverage and short period surface wave observations.

At 112.5 and 175 km depth, the amplitude of the lithospheric velocity anomaly is more similar across models, but S40RTS still has lower peak-to-peak amplitude. The most prominent feature at these depths is that SAVANI-US has significantly more short-wavelength structure (Figs 4 and S4), particularly under North America and the eastern Pacific Ocean. At 275 km depth, SAVANI-US still has substantial short wavelength structure under North America, but the structure under the Pacific Ocean is more consistent with S40RTS while SAVANI and S362ANI + M have longer wavelength structure, including a prominent low velocity anomaly under the East Pacific Rise. At MTZ depths, 410–670 km, all models show similar structures consisting primarily of a high-velocity anomaly along the western Pacific, but less consistent structure in the eastern Pacific. The major difference at these depths is in the S362ANI + M model which has a smooth low velocity anomaly along the eastern Pacific. In the mid-mantle, at 1225 km depth, SAVANI, S40RTS and SAVANI-US all show similar structure whereas S362ANI + M is smoother and shows overall more positive anomalies. As SAVANI, S40RTS and SAVANI-US all use the S + phases of Ritsema *et al.* (2011), this suggests the structure at this depth is largely dependent on the core bouncing and core traversing phases unique to that data set as free-surface reflection phases are also in the data by Lai *et al.* (2019) and the turning depths of those phases are typically within the upper 1000 km. Near the core–mantle boundary, 2775 km depth, the models show the large low shear velocity provinces under the Pacific Ocean and Africa. While the specific geometry varies with each model, the structures are generally in agreement. Overall, SAVANI-US is broadly consistent with previous models at the global scale but presents, expectedly, more short-wavelength structure under North America where USArray data provides high data density.

Radial anisotropy, here defined as $\xi = (V_{sh}/V_{sv})^2$, is significant in the uppermost mantle and provides a complementary view of the Earth structure (e.g. Kustowski *et al.* 2008; Ekström 2011; French & Romanowicz 2014), but it is typically less well constrained

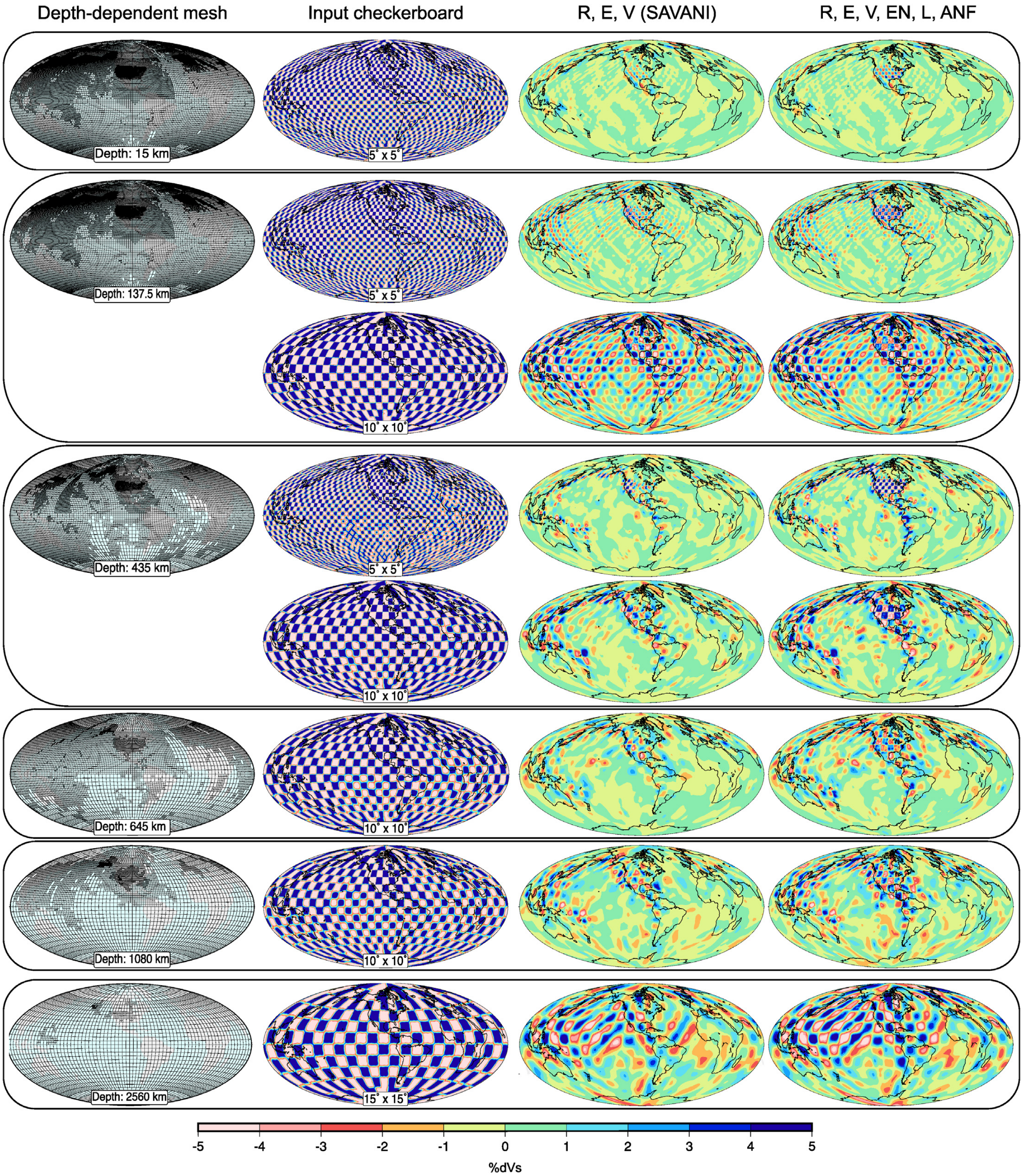

Figure 2. Global scale checkerboard resolution tests. Boxes are used to indicate common depth slices. Left-hand column depicts the depth-dependent mesh centred on the Americas with the depth indicated at the bottom. Minimum size of a voxel is 0.3125° × 0.3125° and maximum size is 5° × 5°. Second column from the left is the input checkerboard at that depth. Radial extent of each checker is six layers and the thickness of each layer varies with depth: ~10 km through the crust, ~50 km through the lithosphere and ~150 km through the mid to lower mantle. Third from the left is the test using only data used in Auer *et al.* (2014) aside from the higher order modes from Visser *et al.* (2008). This data includes Ritsema *et al.* (2011) (R), Ekström (2011) (E) and Visser *et al.* (2008) (V). Right hand column is the test for the new model including additional data from Ekström (2014, 2017) (EN), Lai *et al.* (2019) (L) and the Array Network Facility (ANF).

than isotropic structure with which it trades-off (e.g. Moulik & Ekström 2014). Fig. 5 compares radial anisotropy from SAVANI-US with SAVANI, SEMUCB-WM1 (French & Romanowicz 2014), S362ANI + M and SGLOBE-rani (Chang *et al.* 2015) at the global scale. The models are quite different at 45 km depth, reflecting differences in the background model as SAVANI, SAVANI-US and SGLOBE-rani use an anisotropic version of PREM, SEMUCB-WM1 uses a modified version of PREM, and S362ANI + M uses

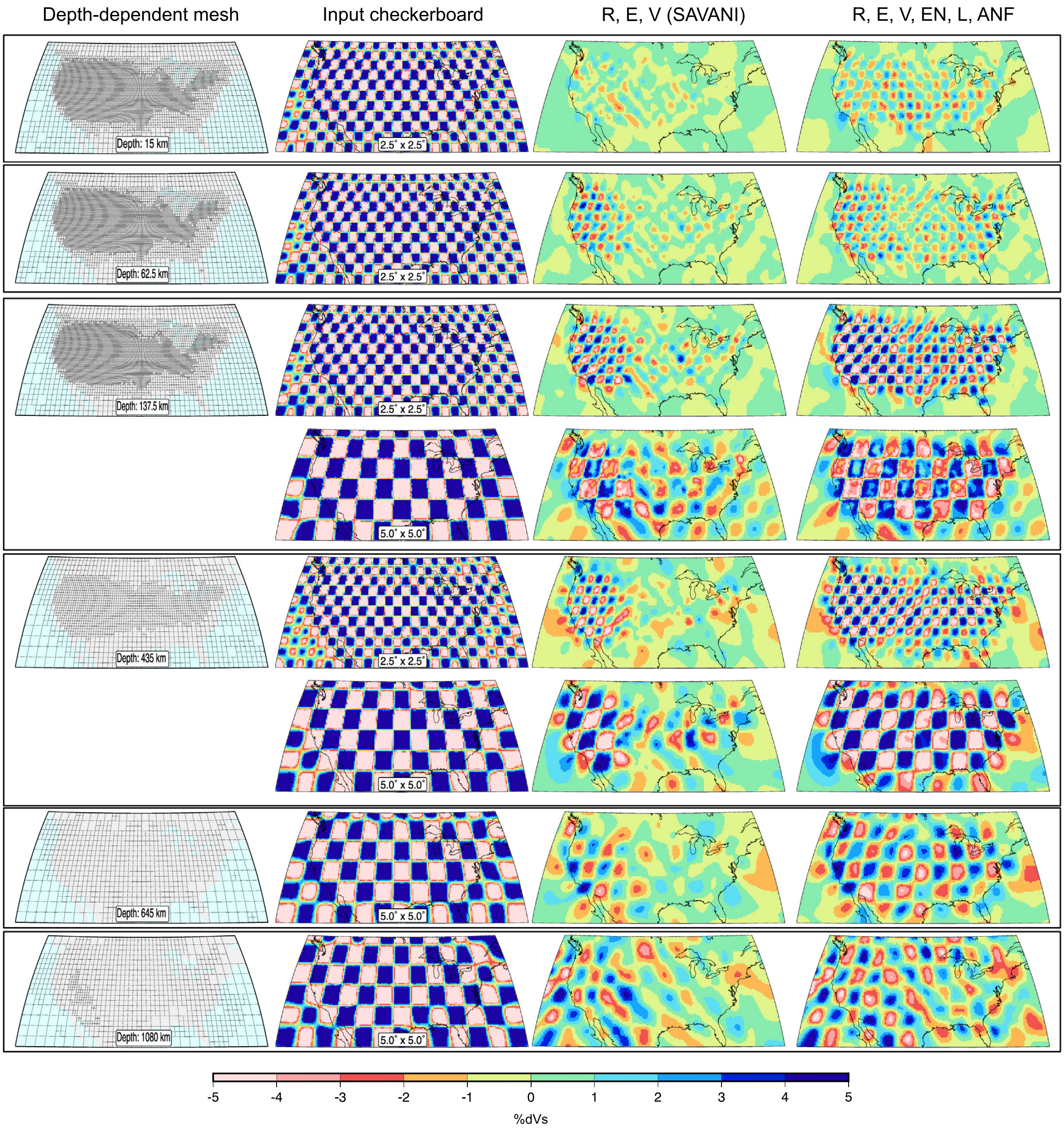

Figure 3. Contiguous United States scale checkerboard resolution tests. Labelling is as Fig. 2.

Table 2. Summary comparison of key attributes of models discussed in Figs 4–6.

Model name	Data type	Scope	Inversion type	Isotropic/anisotropic
SAVANI-US	Body and Surface wave	Global—US Focused	Joint travel time	Anisotropic
SAVANI	Body and Surface wave	Global	Joint travel time	Anisotropic
S40RTS	Normal modes, body waves, surface waves	Global	Joint travel time	Isotropic
S362ANI + M	Normal modes, body waves, surface waves	Global	Joint travel time	Anisotropic
SEMUCB-WM1	Primarily Surface wave	Global	Full waveform	Anisotropic
SGLOBE-rani	Surface wave (fundamental mode and up to 6th overtone)	Global	Travel time	Anisotropic
SL14	Primary body wave	Regional	surface wave to estimate the crust, then body wave	Isotropic
MITS18	Body and Surface wave	Global—US Focused	Iterative joint body wave/surface wave	Isotropic
NASEM	Primarily Surface wave	Global—US Focused	Full waveform in model box	Anisotropic

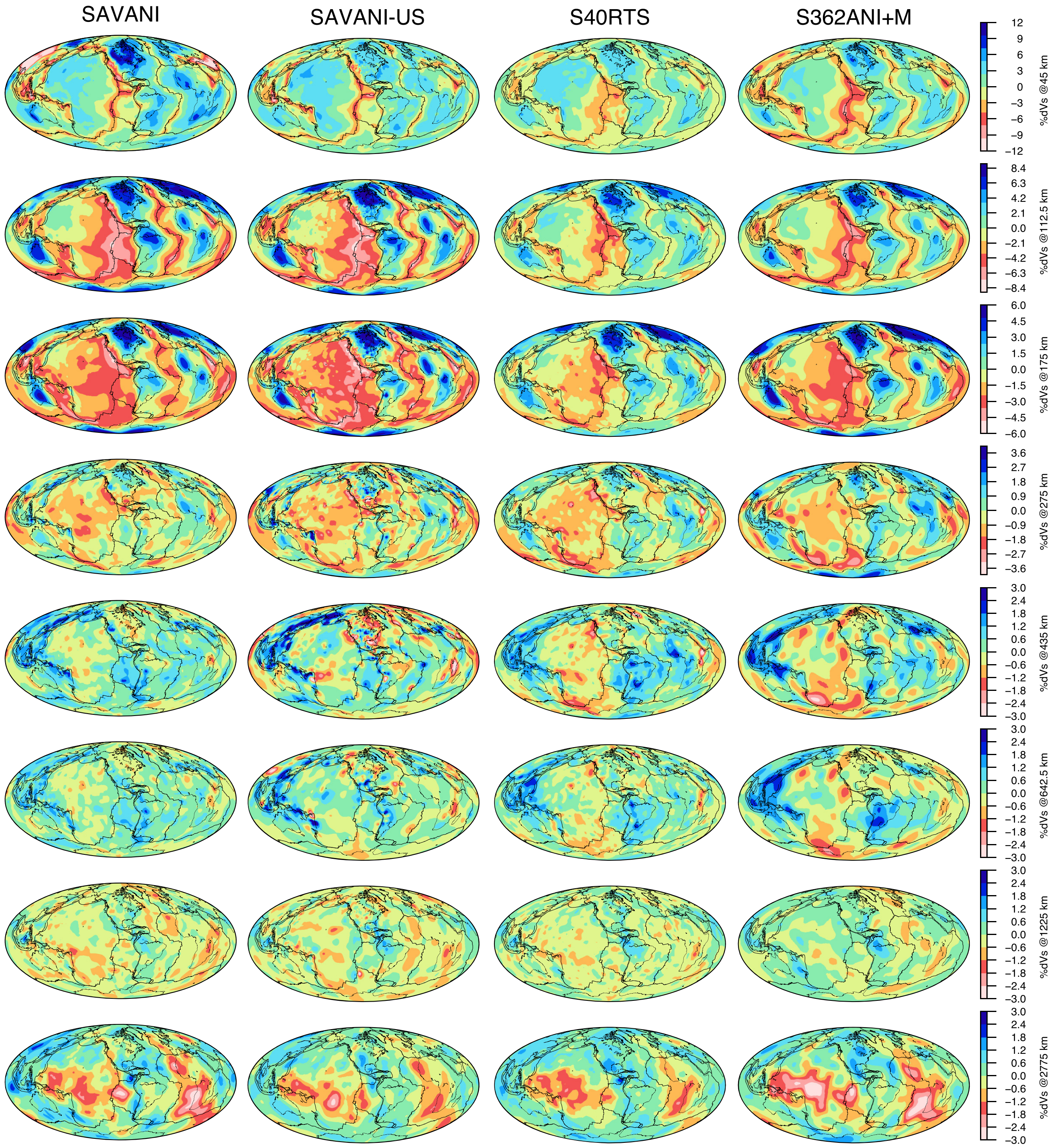

Figure 4. Map view comparison of global model isotropic shear velocity. Each column represents one model and each row is a depth slice with a common colour scale indicated on the right. Left-hand column is SAVANI (Auer *et al.* 2014), second from left is SAVANI-US (this study) third from left is S40RTS (Ritsema *et al.* 2011), and the right-hand column is S362ANI + M (Moulik & Ekström 2014).

KST105 (Kustowski *et al.* 2008) and shallow sensitivity at this depth is globally limited and complicated by the effects of the crust (e.g. Boschi & Ekström 2002). Between 112.5 and 175 km, ξ patterns between all models show some consistent features including $\xi > 1$ in the central Pacific and $\xi < 1$ underneath the East Pacific Rise (e.g. Ekström & Dziewonski 1998). The specific depths where anomalies are found are variable between models, but this is typical of the relatively larger discrepancies between radially anisotropic models compared to isotropic models (*cf.* Moulik & Ekström 2014; Auer *et al.* 2014; Chang *et al.* 2015). Anisotropy at depths larger than ~300 km is significantly dependent on model damping (e.g. Kustowski *et al.* 2008), and in our case the lack of normal modes

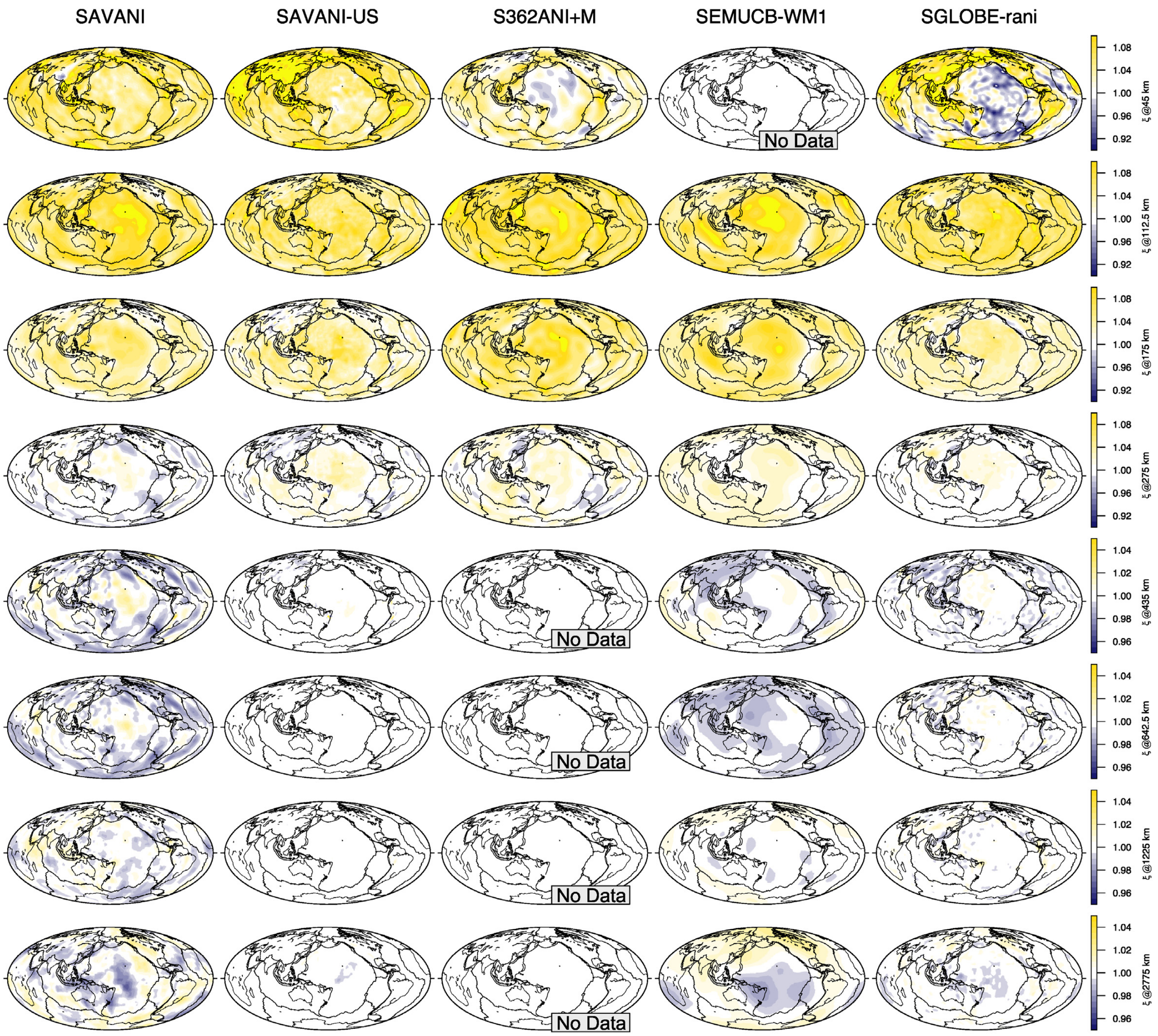

Figure 5. Map view comparison of global model radial anisotropy $(V_{sh}/V_{sv})^2$. Each column represents one model and each row is a depth slice with a common colour scale indicated on the right. Left-hand column is SAVANI (Auer *et al.* 2014), second from left is SAVANI-US (this study), centre is S362ANI + M (Moulik & Ekström 2014), the second from the right-hand column is SEMUCB-WM1 (French & Romanowicz 2014), and the right-most column is SGLOBE-rani (Chang *et al.* 2015).

which limits our resolution compared to SAVANI. This is probably best illustrated by comparing SAVANI and SEMUCB-WM1 at 2775 km depth: SEMUCB-WM1 has long-wavelength structure with $\xi < 1$ at the large low shear velocity provinces and $\xi > 1$ along the edges while SAVANI displays short-wavelength features within that same general long-wavelength pattern. However, as discussed by Chang *et al.* (2015), lower mantle structure is subject to significant isotropic/anisotropic leakage and therefore interpretations should be cautious.

5 REGIONAL SCALE STRUCTURE UNDER THE CONTIGUOUS UNITED STATES

Regional scale models are compared in Fig. 6 to investigate the structure under the contiguous United States. Of these, SL14 (Schmandt & Lin 2014) and MITS18 (Golos *et al.* 2018) are traveltime based models while NASEM (Clouzet *et al.* 2018) is a waveform inversion model based on a regionalization of the method developed for SEMUCB-WM1. While both SL14 and MITS18 use both body wave and surface wave traveltimes, their inversion methodologies differ significantly. SL14 uses Rayleigh wave data to generate a starting model of the crust and uppermost mantle which is held fixed during subsequent inversions of the body wave data whereas MITS18 uses an explicit joint inversion of body wave and surface wave data. This difference leads to notably smoother structure in the shallow part of MITS18 where the laterally propagating surface wave data have more sensitivity than the body wave data. NASEM is the longest wavelength of these models.

The structure at 25 and 45 km depth is largely dependent on the short to intermediate period surface wave data. While both MITS18 and SAVANI-US use the same short period ambient noise data from

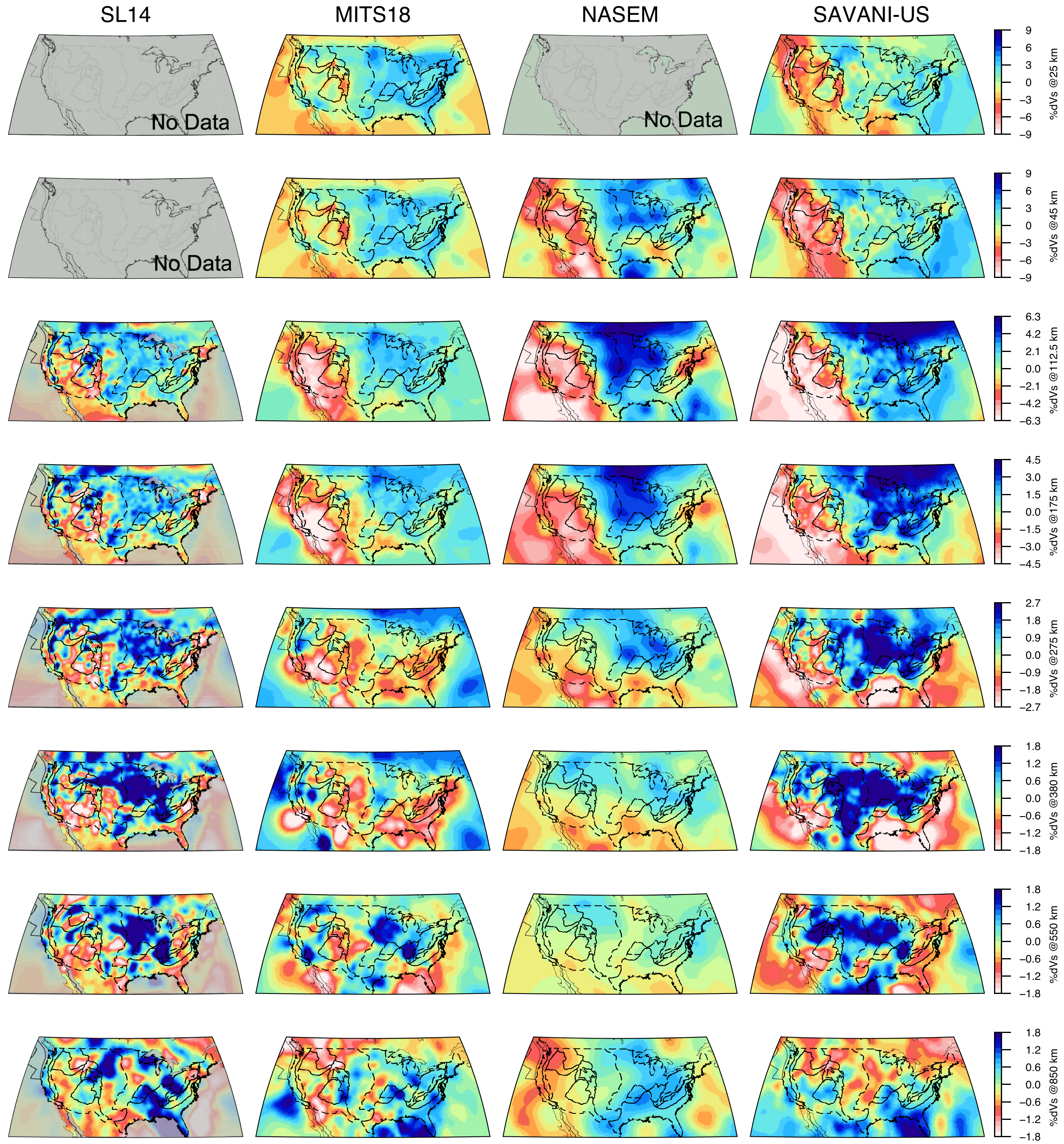

Figure 6. Map view comparison of regional United States velocity models. Each column represents one model and each row is a depth slice with a common colour scale indicated on the right. Left-hand column is SL14 (Schmandt & Lin 2014), second from left is MITS18 (Golos *et al.* 2018), third from left is NASEM (Clouzet *et al.* 2018), and the right-hand column is SAVANI-US (this study).

Ekström (2014, 2017), there are substantial differences in the model results. For example, the west coast and Basin and Range province appear as low velocity anomalies in SAVANI-US, but these regions are neutral to high velocity in MITS18. Differences may arise from the treatment of the intermediate to long period (∼40–290 s) surface wave data. In the case of MITS18, that data is Rayleigh wave measurements from Schaeffer & Lebedev (2014) which solved for V_{sv} and associated azimuthal anisotropy, but in the case of SAVANI-US, the data is Rayleigh and Love wave measurements from Ekström (2011) and Visser *et al.* (2008) which also have been corrected for azimuthal anisotropy. At 45 km depth, the low velocity western United States of SAVANI-US and NASEM appear similar, but the central and eastern United States of SAVANI-US is lower amplitude than NASEM, more similar to MITS18. At 112.5 km depth, SL14 is an outlier as it has shorter wavelength structure than the others, but the contrast between low velocity western United States and high velocity eastern United States is apparent across all models. Deeper in the mantle lithosphere and asthenosphere, NASEM remains the longest wavelength of these models while the visual correlation between SL14 and SAVANI-US increases. For example, both models show high velocity anomalies associated with the Juan de Fuca slab along the west coast, a low velocity feature along the Gulf of Mexico coastline, and a high velocity feature in central Texas adjacent to the rest of the craton. Approaching MTZ depths, 380–550 km, SL14, NASEM and SAVANI-US show largely high velocity features throughout, but MITS18 exhibits more isolated low velocity anomalies. The cause of this difference is unclear, but MITS18 provides a view of the contiguous United States where the cratonic lithosphere is ∼175 km thick and there is an asthenosphere layer which is distinguishable from the lithosphere, slab and transition zone which are all possibly smeared together in the other models. Below the MTZ, at 850 km depth, there are more isolated high velocity anomalies, likely associated with subduction of the FS system. Overall, SAVANI-US is able to capture much of the long wavelength structure seen in NASEM and the short wavelength structure of SL14, roughly on par with MITS18, but the specifics of the data and inversion methodology provide a complementary structural view (also see Figs S7 and S8).

The radial anisotropy structure under the contiguous United States (Fig. S5) is relatively long wavelength in the four models compared (SAVANI, SAVANI-US, S362ANI + M and NASEM). Throughout most of the lithosphere in SAVANI, SAVANI-US and NASEM, ξ is greater than unity whereas S362ANI + M has a large region with ξ less than unity in the central and eastern United States in the crust. In the lower lithosphere, 175–275 km, ξ approaches isotropy in all models. In the rest of the upper mantle, SAVANI-US and S362ANI + M have little perturbations in ξ, possibly due to their damping at those depths while SAVANI shows $\xi < 1$ around the edges of the contiguous United States an NASEM has slightly $\xi > 1$ at 380 km and $\xi < 1$ at 550 km. While this $\xi < 1$ structure in SAVANI might be required by the data, it does correlate with the isotropic structure suggesting there may be some leakage between the isotropic and radially anisotropic structures.

6 DISCUSSION

The mantle structure underneath the contiguous United States results from multiple superimposed geological processes. Arguably, the primary driver of these processes has been subduction of the FS system along the west coast of North America. Multiple episodes of orogenesis and volcanism from this subduction system led to the uplift of the Rocky Mountains, emplacement of the Sierra Nevada pluton and ongoing volcanism in the Cascades Arc. Extension in the Basin and Range province and translation along the San Andreas Fault may be results of subduction of the Pacific-Farallon spreading centre and the subsequent slab window. This destabilization may have also resulted in several lithospheric drips or delamination events such as the Isabella Anomaly (IA), Nevada Anomaly (NA, e.g. West *et al.* 2009), Siletzia Curtain (SC, Schmandt & Humphreys 2011), Wallowa Anomaly (WA, Darold & Humphreys 2013) and roots of the Colorado Plateau (e.g. West *et al.* 2009; Obrebski *et al.* 2011; Levander *et al.* 2011). However, the specific origins of these features remain debatable as models of stalled slabs or depleted asthenospheric mantle may also account for the observed high velocity anomalies. The eastern United States is tectonically stable, but local zones of seismicity such as the New Madrid Seismic Zone (NMSZ, e.g. Nyamwandha *et al.* 2016, and references therein), Eastern Tennessee Seismic Zone (e.g. Powell *et al.* 1994) and the South Carolina Seismic Zone (e.g. Bollinger 1972) suggest there is ongoing deformation. Addressing the geometry and velocity anomalies of these features in SAVANI-US provides new insights into the relevant geological processes.

6.1 The FS system

The geometry of the FS system remains debated. Pavlis *et al.* (2012) provides a summary of several tomographic models and the inferred slab geometry from those, and most seem to indicate a shallowly northeast dipping continuous slab. This model requires a slow slab sinking rate, possibly due to increased viscosity through the Mantle Transition Zone (MTZ) or, maybe more likely, a period of flat-slab subduction, and assumes the apparent gaps in the slab in individual models are either limitations from the tomographic method or are anomalies which developed while the slab was within the asthenosphere. An alternative model was put forward by Sigloch & Mihalynuk (2013) who suggest multiple episodes of intra-oceanic subduction. In this case, the FS system appears discontinuous because it is made up of several smaller oceanic plates, similar to the modern Gorda, Juan de Fuca and Explorer plates.

Cross-sections through our new model, SAVANI-US, are presented in Figs 7, S7 and S8. Section A–A′ in Fig. 7 follows the dip of the modern Gorda-Juan de Fuca system presenting a view of near continuous, largely horizontal subduction from the coast to the high Rocky Mountains, a possible slab gap at the cordillera–craton transition, and then a deeper slab below the transition zone in the eastern United States. As argued by Pavlis *et al.* (2012) this can present a skewed image as the long-term dip direction is approximately towards the northeast from the translational margin in the southwest to the lower mantle as imaged by earlier global tomographic models (*cf.* Tan *et al.* 2002). Nonetheless, this view highlights the major trends. The western limit is relatively steeply dipping, consistent with relatively simple models of modern ocean–continent subduction. Under the cordillera, east of the arc, the shallow mantle is strongly low velocity with a high velocity anomaly in the transition zone. Further east, the high velocity lithosphere of the Laurentia Craton (LC) is relatively distinct in the upper 150–250 km and well separated from the subtransition zone FS.

The perplexing part of cross-section A–A′ (Fig. 7b) is near the centre as a low amplitude, high velocity anomaly extends from the cratonic mantle towards the middle of the transition zone. We do not interpret this as actual lithosphere of vast thickness, but we likely see multiple superimposed anomalies, and the depth separation between them appears difficult to resolve. A resolution test indeed shows that our model-data combination cannot reliably image vertically separated, horizontal fast anomalies in this region (Fig. S6). A comparison of published models along the same cross-section (Fig. S7) shows that other global-scale models image continuous lithosphere in the region that is thinner on average than for our model, but shows some indication of thickening or vertically detached, deeper, fast anomalies in the MTZ in the central part of the profile. Global *P*-wave models and the high resolution, regional model SL14 show faint to distinct, fast anomalies throughout much of the upper mantle in the same region. This might indicate that there are anomalies, perhaps associated with subduction or

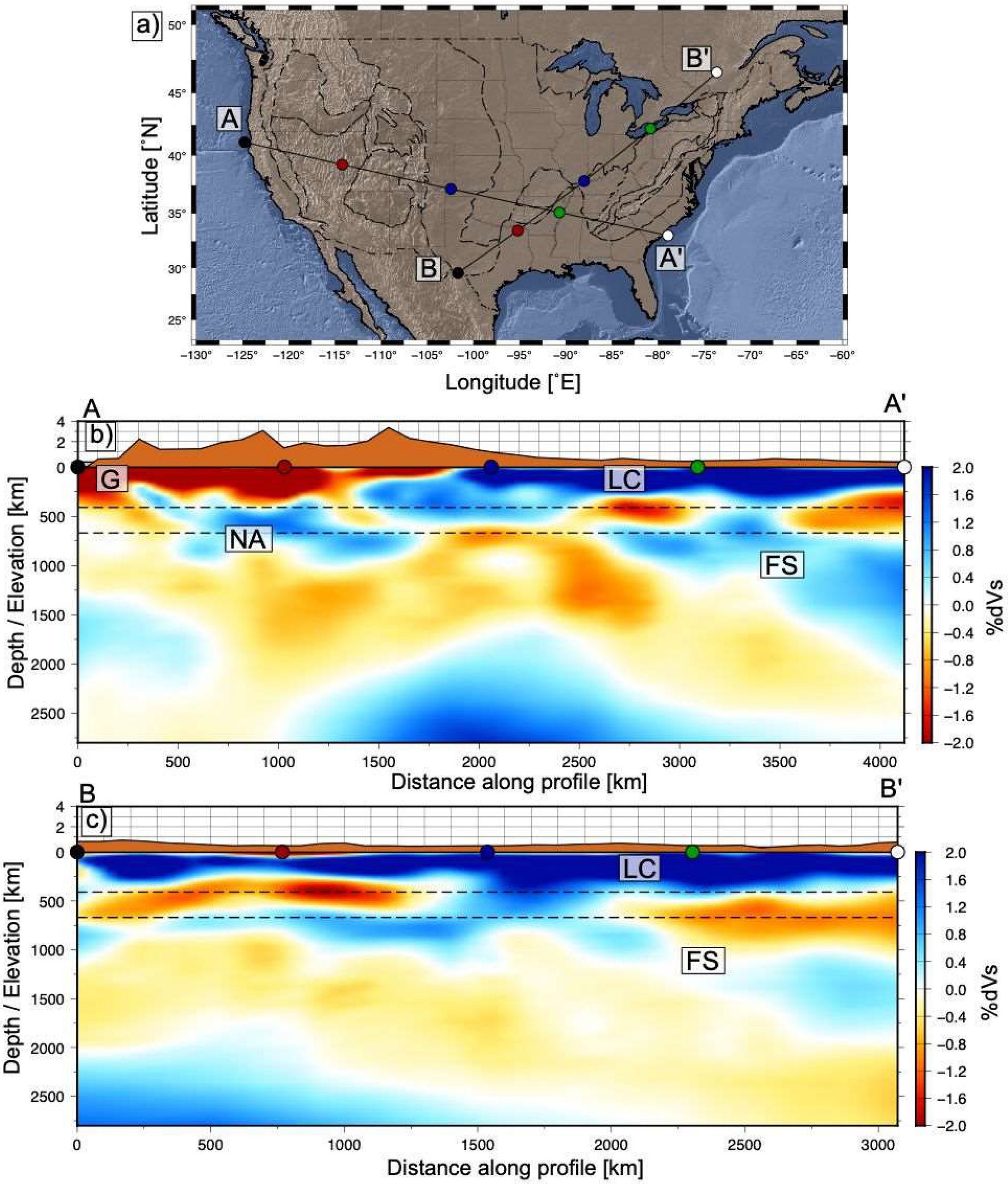

Figure 7. Cross sections along strike and dip of the Farallon system. Labelled features include the Gorda slab (G), Nevada Anomaly (NA), Laurentia Craton (LC) and Farallon Slab (FS). Dashed black lines indicate the Mantle Transition Zone at 410 and 670 km depth. Vertical exaggeration varies with each section. Panel (a) is the location map for lines A–A′ and B–B′. Asymmetrically coloured dots on the lines correspond to the surface projections of the same points on the cross-sections. Panel (b) is roughly along the southern edge of the system and panel (c) is along dip of the centre to eastern portion of the slab.

lithospheric delamination, in the MTZ which are of geodynamic interest, but more work is needed to further enhance structural models and explore the origin of discrepancies between different approaches.

Section B–B′ (Fig. 7c) provides a complementary view. The high velocity LC is apparent throughout and well-separated from the FS in the northeast. Near the northern edge of the Mississippi Embayment the slab shallows and is indistinct from the lithosphere but is separated from the lithosphere in the southwest by a low velocity feature through the MTZ. Notably, in both cross-sections, the FS appears to steepen under the Appalachian Mountains and east coast.

6.2 Stalled slabs and lithospheric instabilities

High velocity anomalies, distinct from active subduction, have long been imaged in the western United States (e.g. Boyd *et al.* 2004; Levander *et al.* 2011). Four of these features are shown in Fig. 8, with the most well explored example, the IA, in Fig. 8(b). The debate over the origin of the IA primarily considers two different models: either an east to west delamination of the Sierra Nevada lithosphere (e.g. Bernardino *et al.* 2019, and references therein) or a captured microplate, the Monterrey Microplate (e.g. Jiang *et al.* 2018 and references therein), which is attached to the Pacific Plate.

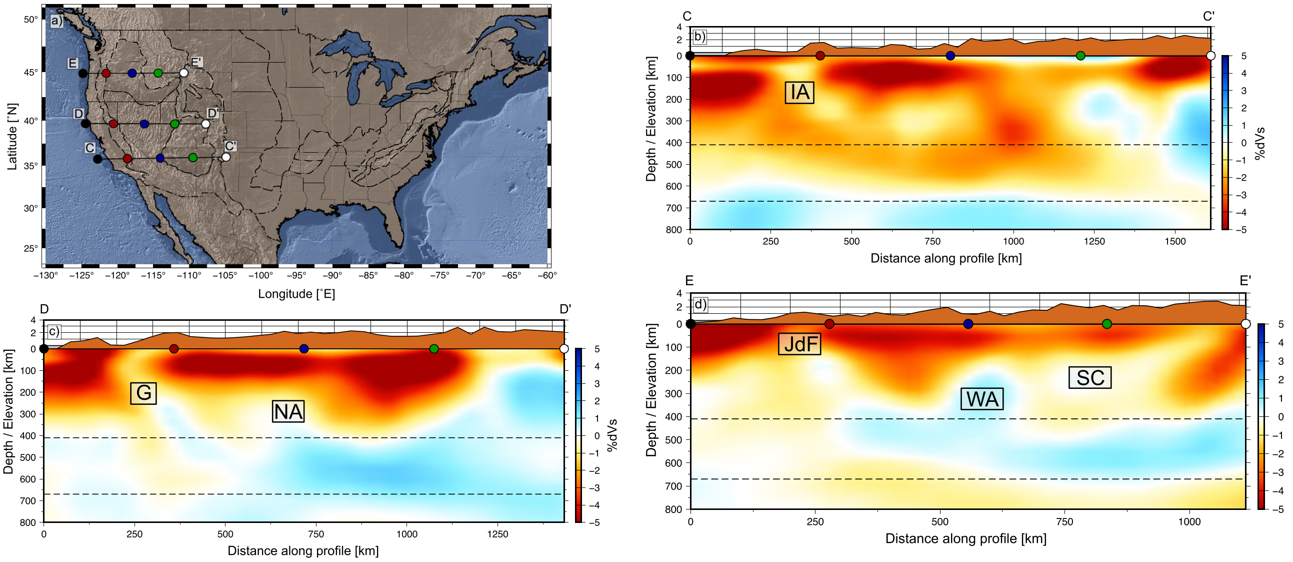

Figure 8. Illustration of reported lithospheric instabilities or stalled slabs. Labelled features include the Juan de Fuca slab (JdF), Siletzia Curtain (SC), Wallowa Anomaly (WA), Gorda slab (G), Nevada Anomaly (NA) and Isabella Anomaly (IA). Panel (a) is the location map for lines C–C′, D–D′ and E–E′. Asymmetrically coloured dots on the lines correspond to the surface projections of the same points on the cross-sections. Dashed black lines indicate the Mantle Transition Zone at 410 and 670 km depth. Vertical exaggeration varies with each section. Panel (b) shows the Isabella Anomaly, panel (c) crosses the Gorda Plate and Nevada Anomaly (West *et al.* 2009) and panel (d) goes through the Juan de Fuca slab, Wallowa Anomaly and Siletzia Curtain (Schmandt & Humphreys 2011).

In SAVANI-US, the IA appears as a relatively neutral velocity surrounded by low velocity anomalies (Fig. 8b). As we would expect a slab or continental lithosphere to be a significantly high velocity anomaly (dV_s $\sim$2 per cent depending on plate age), we can infer that it may have been altered while in the asthenosphere.

Cross-sections D–D′ (Fig. 8c) and E–E′ (Fig. 8d) show that the Gorda slab and Juan de Fuca slab appear geometrically similar to the IA in the western extent, but the transition zone structures in the centre of the cross-sections are significantly different. The maximum depth of the NA in SAVANI-US is mostly consistent with previous studies (e.g. West *et al.* 2009; Obrebski *et al.* 2010; James *et al.* 2011), but the shallow limit of the anomaly only reaches $\sim$250 km depth in SAVANI-US compared with $\sim$50–100 km depth in the NWUS family of models explored in West *et al.* (2009) and James *et al.* (2011). As surface wave data has significant sensitivity to this depth range and the NWUS models use only body-wave data, we expect the shallow high velocity anomalies in the NWUS models are primarily due to smearing of anomalies along the raypath. This raypath effect may also contribute to the apparent differences between SAVANI-US, cross-section E–E′ and Schmandt & Humphreys (2011) when addressing the WA and SC (also see Fig. S8). In Schmandt & Humphreys (2011), the WA is observed attached to the lithosphere and its maximum depth is above the MTZ while in SAVANI-US, the WA appears detached from the lithosphere and is continuous with a high velocity feature within the MTZ. The SC is a steeply dipping high velocity anomaly in Schmandt & Humphreys (2011) which extends into the MTZ, but the feature is roughly horizontal and nearly neutral velocity in SAVANI-US.

High velocity western United States anomalies in SAVANI-US are primarily located within the MTZ. This is consistent with several regional models, and some have explored possible implications of this such as James *et al.* (2011) who proposed edge flow around a slab fragment feeding the Yellowstone Hotspot, and Liu & Stegman (2012) who suggest the segmented slab allowed mantle flow from below the slab fragment. However, assuming these anomalies represent relatively cold and dense fragments of oceanic lithosphere, they should have subducted into the lower mantle. Balancing the chemical, rheological, geometrical and dynamic conditions necessary to support these upper mantle features remains an unsolved problem, but modelling by Burkett & Gurnis (2013), for example, found models may allow for slab stalling of up to $\sim$30 Myr.

In the context of the single slab versus multiple slab endmember subduction models, this lends evidence for the single slab model as we observe several hundred kilometers of approximately continuous high velocity anomalies through the MTZ. The single slab model suggests the Farallon Plate was a large, long-lived oceanic plate analogous to the modern Pacific Plate. Variations in the subduction angle led to episodes of flat slab subduction and periods of steep slab subduction and when the slab reached the base of the MTZ, the increase in viscosity would cause a second phase of slab flattening. Continually subducting this large plate would lead to the observed roughly horizontal high velocity anomalies in the transition zone. The alternative multiple slab model, on the other hand, helps explain some of the features where the slab appears discontinuous. Uncertainties in vertical mass transport and the remaining challenges in resolution mentioned above precludes us from clearly favouring one or the other subduction scenario.

6.3 The New Madrid Seismic Zone

The NMSZ is one of the most active seismic regions in the midcontinent (e.g. Dunn *et al.* 2010, and references therein). As this

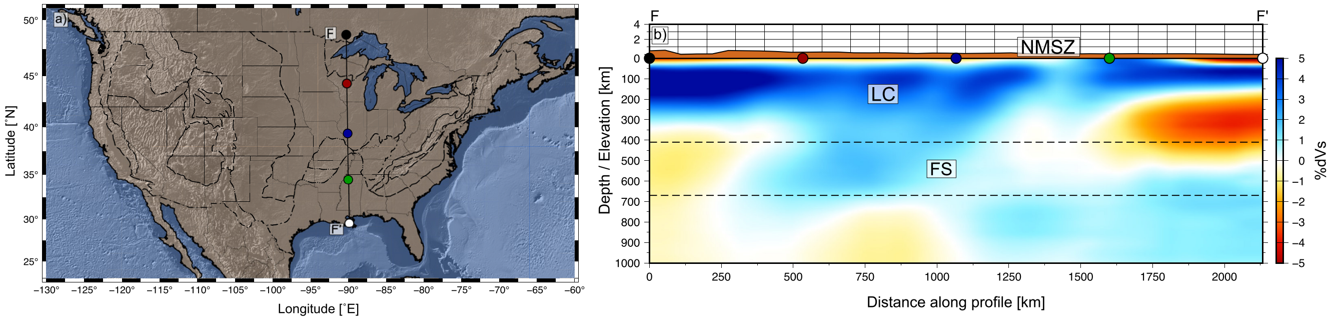

Figure 9. Cross-section through the New Madrid Seismic Zone. Panel (a) is the location map and panel (b) is the north to south cross-section. Labels indicate major features: Laurentia Craton (LC), New Madrid Seismic Zone (NMSZ) and Farallon Slab (FS).

region is far from an active plate boundary, the source of these earthquakes may be attributed to reactivated zones of weakness of the Cambrian-age Reelfoot Rift (Ervin & McGinnis 1975; Hildenbrand & Hendricks 1995). Alternatively, instead of invoking heterogeneity in the lithosphere, mantle loading due to asthenospheric flow may be relevant for determining the location of intraplate seismicity (e.g. Forte *et al.* 2007; Becker *et al.* 2015).

Recent imaging by Nyamwandha *et al.* (2016) finds a pronounced low velocity anomaly at lithospheric depths which they attribute to dewatering from a flat slab segment within the transition zone and suggest the lithosphere was thinned and weakened by passage of a hotspot. Cross-section F–F′ (Fig. 9) shows this structure including a broad high velocity anomaly in the MTZ. In the centre of the cross-section, just north of the NMSZ, the high velocity transition zone structure appears continuous with the overriding craton, but the features separate to the south as the lithosphere thins and the slab deepens. Moreover, the high velocity lithosphere under the NMSZ is only ∼1–2 per cent fast whereas the surrounding lithosphere is ∼3–5 per cent fast. These observations are consistent with the model proposed by Nyamwandha *et al.* (2016) which lacks the mid to lower mantle resolution of SAVANI-US. The slab, however, is seen not to be confined to the MTZ, but rather extends into the top of the lower mantle.

6.4 The eastern United States margin

The eastern United States is a passive margin, but recent studies have shown isolated low velocity lithospheric anomalies (e.g. Porritt *et al.* 2014; Schmandt & Lin 2014; Porter *et al.* 2016; Wagner *et al.* 2018) superimposed on larger-scale high velocity anomalies (e.g. van der Lee *et al.* 2008). The origins of these features remain enigmatic. Fig. 10 illustrates related structures in SAVANI-US. The high velocity lithosphere appears to thin near North Carolina/Virginia (between 750 and 1000 km distance along profile) and southern New England (∼1500 km along profile). Broadly, we expect these features to either be derived from localized mantle upwellings impinging on the base of the lithosphere or inherited structures from initial lithospheric formation. In the former case, we would expect relatively narrow and high amplitude low velocity anomalies where warm material rises, whereas in the latter we would expect long wavelength smoothly varying undulations associated with irregularities in the formation event. Fig. 10 shows these low velocity anomalies are smoothly undulating as expected for inherited structures from the Neoproterozoic accretion of the eastern seaboard terranes. However, we are unable to rule out a later deformation event which has since cooled and left the apparent undulations in lithospheric thickness.

6.5 Dynamic topography

Mantle flow, associated with asthenospheric convection underneath the plate and larger-scale flow, can affect surface topography underneath the western United States (e.g. Forte *et al.* 2007; Liu & Gurnis 2010; Becker *et al.* 2014; Liu 2015). Modelling this dynamic topography requires a global density anomaly model or significant simplifying assumptions to properly estimate mantle flow, and the spatial resolution and confidence in predictions is strongly dependent on the underlying density model, particularly in the uppermost ∼400 km of the mantle. Trying to bridge those scales without having to merge models a posterior is, in fact, what partially motivated the current study.

To illustrate the advance SAVANI-US provides in this respect, we compare the short and long wavelength dynamic topography inferred from three different tomographic models in Fig. 11. These computations are performed using a simplified constant scaling of shear wave velocity anomalies and radial viscosity variations, following the approach of Becker *et al.* (2014), in the exact same way for all three tomographic models. For our purposes, the details of flow modelling do not matter, and results can be viewed as a geodynamically motivated average over the uppermost mantle structure.

The global model, SAVANI, has relatively low resolution under the contiguous United States and this is reflected in the inferred dynamic topography (Fig. 11a); the signature mainly reflects large-scale lithospheric structure, and results are broadly negative across the Rocky Mountains with more neutral to positive values towards the west coast with a divot of neutral dynamic topography at the Yellowstone Hotspot. Embedding the model of Schmandt & Lin (2014) into SAVANI (Fig. 11b), similar to what was done in Becker *et al.* (2015), produces smaller-scale, negative topography anomalies associated with the Juan de Fuca slab, and other high velocity anomalies discussed above (*cf.* Becker *et al.* 2015). Comparing those two models with the new SAVANI-US results (Fig. 11c), we observe the large contrast across the Rocky Mountains as per what is captured in SAVANI alone, and the smaller-scale positive features in the Basin and Range Province and Yellowstone Hotspot as per the embedded model are likewise resolved (*cf.* Fig. 6). SAVANI-US shows similar small-scale features as the merger including Schmandt & Lin's (2014) model, including a north–south oriented negative anomaly along the modern Cascades arc and Juan de Fuca slab, a positive anomaly associated with the Yellowstone Hotspot and eastern Basin

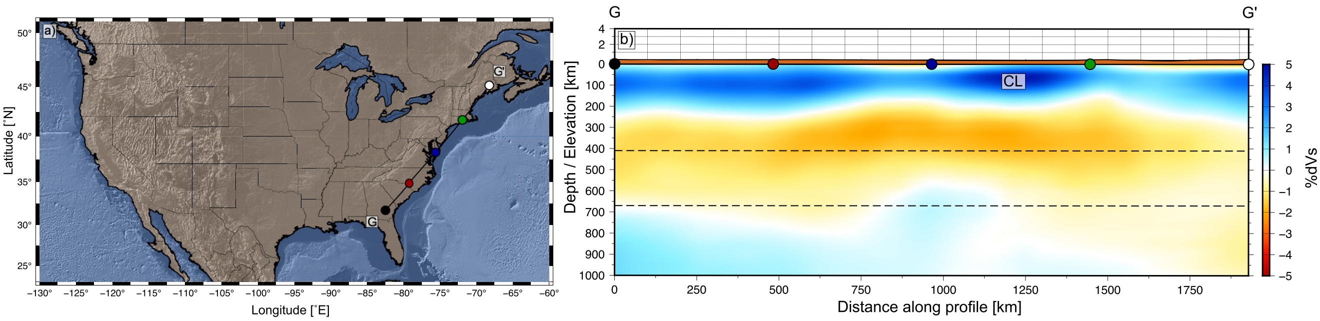

Figure 10. Cross-section through the United States eastern seaboard. Panel (a) is the location map and panel (b) is the cross-section. Continental lithosphere (CL) is labelled.

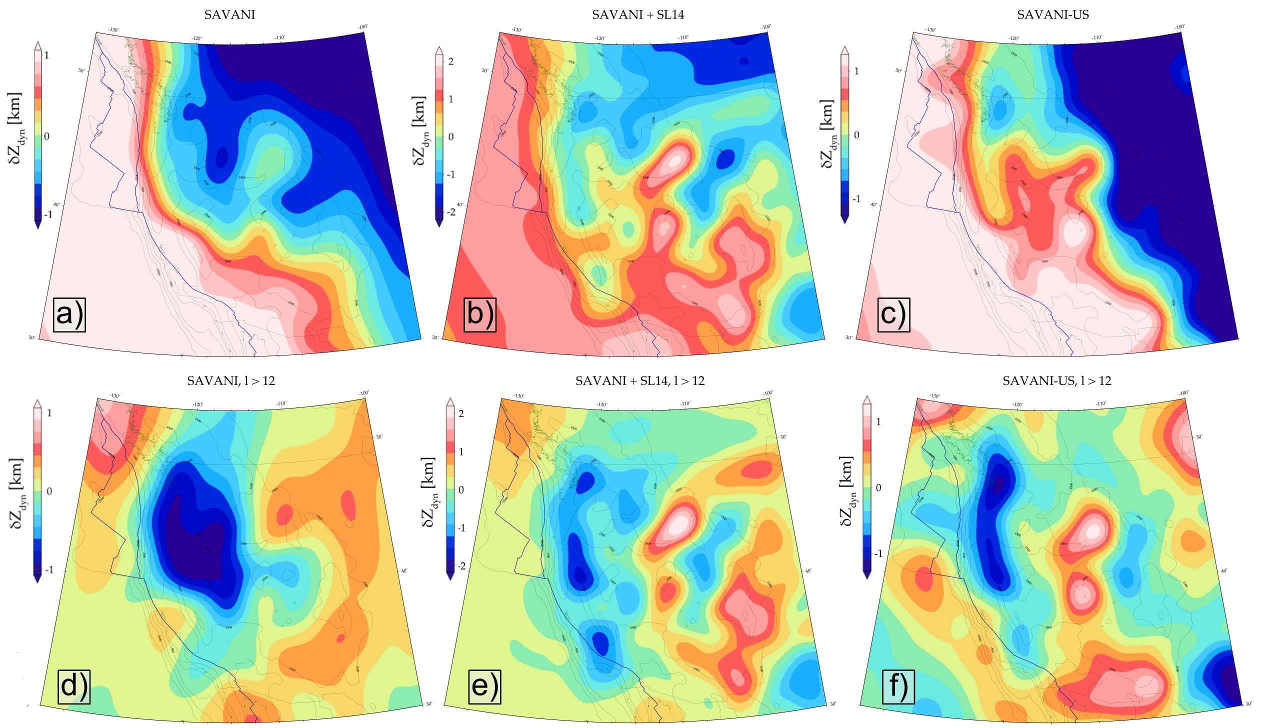

Figure 11. Models of dynamic topography based on density variations inferred from different tomographic models. Top row considers all structural wavelengths available while the bottom row limits the estimates to short wavelengths (spherical harmonic degree, $l > 12$). Panel (a) is based on SAVANI (Auer *et al.* 2014). Panel (b) is a merger of SAVANI for the global structure with Schmandt & Lin (2014). Panel (c) is SAVANI-US. Panels (df) are as (a–c) but low order structures have been filtered out.

and Range, and a positive anomaly along the southern Colorado Plateau (*cf.* Becker *et al.* 2014). There are small, short wavelength differences with the embedded model such as the lack of a positive anomaly in the northern Rio Grande Rift, and this implies that Schmandt & Lin (2014) is still slightly higher resolution than SAVANI-US at those depths. Nonetheless, this comparison shows that SAVANI-US captures a key geodynamic process in a single self-consistent model without the need of posterior assumptions to merge two independent models.

7 CONCLUSIONS

We have produced a new, global, multiscale, radially anisotropic shear wave tomography model for the contiguous United States, SAVANI-United States. SAVANI-US is consistent with previously imaged global scale structure but inclusion of USArray data in the form of teleseismic traveltimes and ambient noise-based dispersion additionally provides regional, high resolution structure similar to what is recovered by regional models. The FS system appears to be discontinuous and shallowly dipping to the east–northeast within the mantle transition zone under the interior of the contiguous United States, with substantially steeper dipping segments along the west coast and under the Appalachian Mountains and further east. In the western United States, previously imaged slabs or delamination events are found to be either lower amplitude or deeper than previously imaged in regional models, likely due to our surface wave constraints. Under the New Madrid Seismic Zone, we find evidence for a north to south transition from a shallow slab, near the base of the lithosphere, to a deeper slab below the transition zone. Along the east coast, the high velocity lithosphere seems to undulate in its thickness and this variation might contribute to apparent low velocity anomalies when viewed in map view. Finally, when using SAVANI-US to model dynamic topography, the model is able to replicate both the long-wavelength, lithospheric features seen based on global tomographic models and the short-wavelength features from regionalized models. As with any model, SAVANI-US has limitations, and while the global scale structure is highly similar to other models, SAVANI-US is not ideal for analysis in the deep mantle where our resolution is currently limited due to a relatively small number of body wave ray paths which travel through the lower mantle. Nonetheless, our improved, cross-scale model reconciles previous estimates of the mantle shear wave structure underneath the contiguous United States from regional and global models. This advances our interpretative capabilities in terms of analysing structure of continental dynamics.

ACKNOWLEDGEMENTS

Seismic data for this study was obtained from the Array Network Facility (https://anf.ucsd.edu/tools/events/), Goran Ekström (https://www.ldeo.columbia.edu/∼ekstrom/Projects/ANT/USANT15/USANT15.html), Jeroen Ritsema (Ritsema *et al.* 2011) and Hongyu Lai and Ed Garnero (Lai *et al.* 2019). All figures made with Generic Mapping Tools (Wessel *et al.* 2013). The model presented here will be made available at the IRIS Earth Model Collaboration website (https://ds.iris.edu/ds/products/emc/) upon publication. We further thank the IRIS Earth Model Collaboration website (Trabant *et al.* 2012) for hosting several of the velocity models compared here and during development and the original authors for providing their models to the website. Software to recreate the model are available at https://github.com/rwporritt/savani, but traveltime data will need to be obtained separately. RWP was partially supported by The Bureau of Economic Geology at UT Austin, and TWB acknowledges NSF EAR-1722680, 1927216 and NASA OSP 201601412-001 as support. RWP gathered the data, prepared and ran the inversions and prepared the paper. TWB designed the research with RWP and LB, and ran the dynamic topography calculations. LB and LA wrote the tomographic inversion software and helped RWP install the software. All authors contributed to interpretation and writing the paper.

REFERENCES

Amaru, M.L., 2007. Global travel time tomography with 3-D reference models, *Geologica Ultraiectina,* **274,** 174p.

Auer, L., Boschi, L., Becker, T.W., Nissen-Meyer, T. & Giardini, D., 2014. Savani: a variable-resolution whole-mantle model of anisotropic shear-velocity variations based on multiple datasets, *J. geophys. Res.,* **119,** 3006–3034, doi:10.1002/2013JB010773.

Balay, S. *et al.*, 2020. *PETSc Users Manual. Argonne National Laboratory*. ANL-95/11 – Revision 3.13.

Becker, T.W., 2012. On recent seismic tomography for the western United States, *Geochem. Geophys. Geosyst.,* **13,** Q01W10, doi:10.1029/2011GC003977.

Becker, T.W. & Boschi, L., 2002. A comparison of tomographic and geodynamic mantle models, *Geochem., Geophys., Geosys.,* **3**(1), 1003, doi:10.1029/2001GC000168.

Becker, T.W., Faccenna, C., Humphreys, E.D., Lowry, A.R. & Miller, M.S., 2014. Static and dynamic support of western United States topography, *Earth planet. Sci. Lett.,* **402,** 234–246.

Becker, T.W., Lowry, A.R., Faccenna, C., Schmandt, B., Borsa, A. & Yu, C., 2015. Western U.S. intermountain seismicity caused by changes in upper mantle flow, *Nature,* **524,** 458–461.

Bedle, H. & van der Lee, S., 2009. S velocity variations beneath North America, *J. geophys. Res.,* **114,** B07308, doi:10.1029/2008JB005949.

Bernardino, M.V., Jones, C.H., Levandowski, W., Bastow, I., Owens, T.J. & Gilbert, H., 2019. A multicomponent Isabella anomaly: Resolving the physical state of the Sierra Nevada upper mantle from Vp/Vs anisotropy tomography, *Geosphere,* **15**(6), 2018–2042.

Bijwaard, H., Spakman, W. & Engdahl, E.R., 1998. Closing the gap between regional and global travel time tomography, *J. geophys. Res.,* **103**(B12), 30055–30078.

Bollinger, G.A., 1972. Historical and recent seismic activity in South Carolina, *Bulletin of the Seismological Society of America,* **62**(3), 851–864.

Boschi, L. & Ekström, G., 2002. New images of the Earth's upper mantle from measurements of surface-wave phase velocity anomalies, *J. geophys. Res.,* **107**(B4), 2059, doi:10.1029/2000JB000059.

Boyce, A., Bastow, I.D., Golos, E.M., Rondenay, S., Burdick, S. & Van der Hilst, R., 2019. Variable modification of continental lithosphere during the Proterozoic Grenville orogeny: evidence from teleseismic P-wave tomography, *Earth planet. Sci. Lett.,* **525,** 115763, doi:10.1016/j.epsl.2019.115763.

Boyd, O.S., Jones, C.H. & Sheehan, A.F., 2004. Foundering lithosphere imaged beneath the Southern Sierra Nevada, California, USA, *Science,* **305**(5684), 660–662.

Bunge, H.P. & Grand, S.P., 2000. Mesozoic plate-motion history below the northeast Pacific Ocean from seismic images of the subducted Farallon slab, *Nature,* **405**(6784), 337–340.

Burdick, S. *et al.*, 2008. Upper mantle heterogeneity beneath North America from travel time tomography with global and USArray Transportable Array data, *Seismol. Res. Lett.,* **79,** 384–390.

Burdick, S. *et al.*, 2017. Model update May 2016: upper-mantle heterogeneity beneath North America from travel-time tomography with global and USArray data, *Seismol. Res. Lett.,* **88,** 319–325.

Burkett, E. & Gurnis, M., 2013. Stalled slab dynamics, *Lithosphere,* **5**(1), 92–97.

Chang, S.J., Ferreira, A.M., Ritsema, J., van Heijst, H.J. & Woodhouse, J.H., 2015. Joint inversion for global isotropic and radially anisotropic mantle structure including crustal thickness perturbations, *J. geophys. Res.,* **120**(6), 4278–4300.

Clennett, E.J. *et al.*, 2020. A quantitative tomotectonic plate reconstruction of western North America and the eastern Pacific basin, *Geochem. Geophys. Geosyst.,* **21,** e2020GC009117. doi:10.1029/2020GC009117.

Clouzet, P., Masson, Y. & Romanowicz, B., 2018. Box tomography: first application to the imaging of upper-mantle shear velocity and radial anisotropy structure beneath the North American continent, *Geophys. J. Int.,* **213**(3), 1849–1875.

Darold, A. & Humphreys, E., 2013. Upper mantle seismic structure beneath the Pacific Northwest: a plume-triggered delamination origin for the Columbia River flood basalt eruptions, *Earth planet. Sci. Lett.,* **365,** 232–242.

Dunn, M., Horton, S., DeShon, H. & Powell, C., 2010. High-resolution earthquake relocation in the New Madrid seismic zone, *Seismol. Res. Lett.,* **81**(2), 406–413.

Dziewonski, A.M. & Anderson, D.L., 1981. Preliminary reference Earth model, *Phys. Earth planet. Inter.,* **25**(4), 297–356.

Ekström, G., 2011. A global model of Love and Rayleigh surface wave dispersion and anisotropy, 25–250 s, *Geophys. J. Int.,* **187**(3), 1668–1686.

Ekström, G., 2014. Love and Rayleigh phase-velocity maps, 5–40 s, of the western and central USA from USArray data, *Earth planet. Sci. Lett.,* **402,** 42–49.

Ekström, G., 2017. Short-period surface-wave phase velocities across the conterminous United States, *Phys. Earth planet. Inter.,* **270,** 168–175.

Ekström, G. & Dziewonski, A.M., 1998. The unique anisotropy of the Pacific upper mantle, *Nature,* **394**(6689), 168–172.

Engdahl, E.R., Di Giacomo, D., Sakarya, B., Gkarlaouni, C.G., Harris, J. & Storchak, D.A., 2020. ISC-EHB 1964–2016, an improved data set for studies of Earth structure and global seismicity, *Earth Space Sci.,* **7**(1), e2019EA000897, doi:10.1029/2019EA000897.

Engdahl, E.R., van der Hilst, R. & Buland, R., 1998. Global teleseismic earthquake relocation with improved travel times and procedures for depth determination, *Bull. seism. Soc. Am.,* **88**(3), 722–743.

Ervin, C.P. & McGinnis, L.D., 1975. Reelfoot rift: reactivated precursor to the Mississippi embayment, *Bull. Geol. Soc. Am.,* **86,** 1287–1295.

Forte, A.M., Mitrovica, J.X., Moucha, R., Simmons, N.A. & Grand, S.P., 2007. Descent of the ancient Farallon slab drives localized mantle flow below the New Madrid seismic zone, *Geophys. Res. Lett.,* **34,** L04308.

French, S.W. & Romanowicz, B.A., 2014. Whole-mantle radially anisotropic shear velocity structure from spectral-element waveform tomography, *Geophys. J. Int.,* **199**(3), 1303–1327.

Fukao, Y. & Obayashi, M., 2013. Subducted slabs stagnant above, penetrating through and trapped below the 660-km discontinuity, *J. Geophys. Res.,* **118**(11), 5920–5938.

Ghosh, A., Becker, T.W. & Humphreys, E.D., 2013. Dynamics of the North American continent, *Geophys. J. Int.,* **194,** 651–669.

Golos, E.M. *et al.*, 2018. Shear wave tomography beneath the United States using a joint inversion of surface and body waves, *J. geophys. Res.,* **123,** 5169–5189.

Grand, S.P., Van der Hilst, R.D. & Widiyantoro, S., 1997. High resolution global tomography: a snapshot of convection in the Earth, *Geol. Soc. Am. Today,* **7**(4), ISSN: 1052-5173.

Hall, R. & Spakman, W., 2015. Mantle structure and tectonic history of SE Asia, *Tectonophysics,* **658,** 14–45.

Hawley, W.B. & Allen, R.M., 2019. The fragmented death of the Farallon plate, *Geophys. Res. Lett.,* **46,** doi:10.1029/2019GL083437.

Hildenbrand, T. & Hendricks, J., 1995. *Geophysical Setting of the Reelfoot Rift and Relations between Rift Structures and the New Madrid Seismic Zone*. USGS Professional Paper 1583.

International Seismological Centre, 2020. *ISC-EHB dataset,* doi:10.31905/PY08W6S3.

James, D.E., Fouch, M.J., Carlson, R.W. & Roth, J.B., 2011. Slab fragmentation, edge flow and the origin of the Yellowstone hotspot track, *Earth planet. Sci. Lett.,* **311**(1–2), 124–135.

Jiang, C., Schmandt, B., Hansen, S.M., Dougherty, S.L., Clayton, R.W., Farrell, J. & Lin, F.-C., 2018. Rayleigh and S wave tomography constraints on subduction termination and lithospheric foundering in central California, *Earth planet. Sci. Lett.,* **488,** 14–26.

Jin, G. & Gaherty, J.B., 2015. Surface wave phase-velocity tomography based on multichannel cross-correlation, *Geophys. J. Int.,* **201,** 1383–1398.

Kustowski, B., Ekström, G. & Dziewonski, A.M., 2008. Anisotropic shear-wave velocity structure of the Earth's mantle: a global model, *J. geophys. Res.,* **113,** B06306, doi:10.1029/2007JB005169.

Lai, H., Garnero, E.J., Grand, S.P., Porritt, R.W. & Becker, T.W., 2019. Global travel time data set from adaptive empirical wavelet construction, *Geochem. Geophys. Geosyst.,* **20,** 2175–2198.

Laske, G., Masters., G., Ma, Z. & Pasyanos, M., 2013. Update on CRUST1.0 - a 1-degree global model of Earth's crust, *Geophys. Res. Abstracts,* **15,** Abstract EGU2013-2658.

Levander, A., Schmandt, B., Miller, M.S., Liu, K., Karlstrom, K.E., Crow, R.S., Lee, C.-T.A. & Humphreys, E.D., 2011. Continuing Colorado plateau uplift by delamination-style convective lithospheric downwelling, *Nature,* **472**(7344), 461–465.

Li, C., van der Hilst, R.D., Engdahl, E.R. & Burdick, S., 2008. A new global model for P wave speed variations in Earth's mantle, *Geochem. Geophys. Geosyst.,* **9**(5), doi:10.1029/2007GC001806.

Liu, L., 2015. The ups and downs of North America: evaluating the role of mantle dynamic topography since the Mesozoic, *Rev. Geophys.,* **53**(3), 1022–1049.

Liu, L. & Gurnis, M., 2010. Dynamic subsidence and uplift of the Colorado Plateau, *Geology,* **38**(7), 663–666.

Liu, L. & Stegman, D.R., 2012. Origin of Columbia River flood basalt controlled by propagating rupture of the Farallon slab, *Nature,* **482,** 386–390.

Lu, C., Grand, S.P., Lai, H. & Garnero, E.J., 2019. TX2019slab: A new P and S tomography model incorporating subducting slabs, *J. Geophys. Res. Solid Earth,* **124,** 11549–11567.

Moulik, P. & Ekstrom, G., 2014. An anisotropic shear velocity model of the Earth's mantle using normal modes, body waves, surface waves and long-period waveforms, *Geophys. J. Int.,* **199**(3), 1713–1738.

Nyamwandha, C.A., Powell, C.A. & Langston, C.A., 2016. A joint local and teleseismic tomography study of the Mississipii Embayment and New Madrid Seismic Zone, *J. geophys. Res.,* **121,** 3570–3585.

Obayashi, M., Yoshimitsu, J., Nolet, G., Fukao, Y., Shiobara, H., Sugioka, H., Miyamachi, H. & Gao, Y., 2013. Finite frequency whole mantle P-wave tomography: Inprovement of subducted slab, *Geophys. Res. Lett.,* **40**(21), 5652–5657.

Obrebski, M., Allen, R.M., Pollitz, F. & Hung, S.-H., 2011. Lithosphere-asthenosphere interaction beneath the western United States from the joint inversion of body-wave traveltimes and surface-wave phase velocities, *Geophys. J. Int.,* **185,** 1003–1021.

Obrebski, M., Allen, R.M., Xue, M. & Hung, S.-H., 2010. Slab-Plume Interaction beneath the Pacific Northwest, *Geophys. Res. Lett.,* **37,** L14305, doi:10.1029/2010GL043489.

Pavlis, G.L., Sigloch, K., Burdick, S., Fouch, M.J. & Vernon, F.L., 2012. Unraveling the geometry of the Farallon plate: synthesis of three-dimensional imaging results from USArray, *Tectonophysics,* **532,** 82–102.

Porritt, R.W., Allen, R.M. & Pollitz, F.F., 2014. Seismic imaging east of the Rocky Mountains with USArray, *Earth planet. Sci. Lett.,* **402,** 16–25.

Porter, R., Liu, Y. & Holt, W.E., 2016. Lithospheric records of orogeny within the continental U.S, *Geophys. Res. Lett.,* **43**(1), 144–153.

Powell, C.A., Bollinger, G.A., Chapman, M.C., Sibol, M.S., Johnston, A.C. & Wheeler, R.L., 1994. A seismotectonic model for the 300-kilometer-long eastern Tennessee seismic zone, *Science,* **264**(5159), 686–688.

Ritsema, J., van Heijst, H.J., Deuss, A. & Woodhouse, J.H., 2011. S40RTS: a degree-40 shear velocity model for the mantle from new Rayleigh wave dispersion, teleseismic traveltimes, and normal-mode splitting function measurements, *Geophys. J. Int.,* **184,** 1223–1236.

Schaeffer, A.J. & Lebedev, S., 2014. Imaging the North American continent using waveform inversion of global and USArray data, *Earth planet. Sci. Lett.,* **402,** 26–41.

Schmandt, B. & Humphreys, E., 2010. Complex subduction and small-scale convection revealed by body-wave tomography of the western United States mantle, *Earth planet. Sci. Lett.,* **297,** 435–445.

Schmandt, B. & Humphreys, E., 2011. Seismically imaged relict slab from the 55 Ma Siletzia accretion to the northwest United States, *Geology,* **39**(2), 175–178.

Schmandt, B. & Lin, F.-C., 2014. P and S wave tomography of the mantle beneath the United States, *Geophys. Res. Lett.,* **41,** doi:10.1002/2014GL061231.

Sigloch, K., 2011. Mantle provinces under North America from multifrequency P wave tomography, *Geochem. Geophys. Geosyst.,* **12**(2), doi:10.1029/2010GC003421.

Sigloch, K. & Mihalynuk, M., 2013. Intra-oceanic subduction shaped the assembly of Cordilleran North America, *Nature,* **496,** 50–56.

Simmons, N.A., Forte, A.M., Boschi, L. & Grand, S.P., 2010. GyPSuM: a joint tomographic model of mantle density and seismic wave speeds, *J. geophys. Res.,* **115,** B12310. doi:10.1029/2010JB007631.

Tan, E., Gurnis, M. & Han, L., 2002. Slabs in the lower mantle and their modulation of plume formation, *Geochem. Geophys. Geosyst.,* **3**(11), 1067, doi:10.1029/2001GC000238.

Trabant, C., Hutko, A.R., Bahavar, M., Karstens, R., Ahern, T. & Aster, R., 2012. Data products at the IRIS DMC: stepping stones for research and other applications, *Seismol. Res. Lett.,* **83**(5), 846–854.

van der Lee, S. & Frederiksen, A., 2005. Surface wave tomography applied to the North American upper mantle, in *AGU Monograph. Seismic Earth: Array Analysis of Broadband Seismograms,* Geophysical Monograph Series, pp. 67–80, eds Levander, A. & Nolet, G., doi:10.1029/157GM05, American Geophysical Union.

van der Lee, S., Regenauer-Lieb, K. & Yuen, D.A., 2008. The role of water in connecting past and future episodes of subduction, *Earth planet. Sci. Lett.,* **273**(1–2), 15–27.

VanDecar, J.C. & Crosson, R.S., 1990. Determination of teleseismic relative phase arrival times using multi-channel cross-correlation and least squares, *Bull. seism. Soc. Am.,* **80**(1), 150–169.

Visser, K., Trampert, J. & Kennett, B.L.N., 2008. Global anisotropic phase velocity maps for higher mode Love and Rayleigh waves, *Geophys. J. Int.,* **172**(3), 1016–1032.

Wagner, L.S., Fischer, K.M., Hawman, R., Hopper, E. & Howell, D., 2018. The relative roles of inheritance and long-term passive margin lithospheric evolution on the modern structure and tectonic activity in the southeastern United States, *Geosphere,* **14**(4), 1385–1410.

Wang, W. & Becker, T.W., 2019. Upper mantle seismic anisotropy as a constraint for mantle flow and dynamics of the North American plate, *Earth planet. Sci. Lett.,* **514,** 143–155.

Wessel, P., Smith, W.H.F., Scharroo, R., Luis, J.F. & Wobbe, F., 2013. Generic Mapping Tools: improved version released, *EOS, Trans. Am. geophys. Un.,* **94,** 409–410.

West, J., Fouch, M., Roth, J. & Elkins-Tanton, L.T., 2009. Vertical mantle flow associated with a lithospheric drip beneath the Great Basin, *Nat. Geosci*., **2,** 439–444.

Weston, J., Engdahl, E.R., Harris, J., Di Giacomo, D. & Storchack, D.A., 2018. ISC-EHB: reconstruction of a robust earthquake dataset, *Geophys. J. Int.,* **214**(1), 474–484.

Woodhouse, J., 1981. A note on the calculation of travel times in a transversely isotropic Earth model, *Phys. Earth planet. Inter.,* **25**(4), 357–359.

Xue, M. & Allen, R.M., 2007. The fate of the Juan de Fuca plate: implications for a Yellowstone plume head, *Earth planet. Sci. Lett.,* **264**(1–2), 266–276.

Yuan, H. & Romanowicz, B., 2010. Lithospheric layering in the North American craton, *Nature,* **466**(7310), 1063–1068.

Zhou, Q., Liu, L. & Hu, J., 2018. Western US volcanism due to intruding oceanic mantle driven by ancient Farallon slabs, *Nat. Geosci.,* **11**(1), 70–76.

SUPPORTING INFORMATION

Supplementary data are available at *GJI* online.

Table S1. Full summary of the data set used in the inversion for SAVANI-US.

Figure S1. Data adaptive mesh used for the tomographic inversion at each model layer. Bottom of each panel indicates the depth. This mesh was created with the SAVANI software available at https://github.com/rwporritt/savani. Specifically, this depends on hit count adaptive for each voxel. The minimum voxel size is set to 0.3125° × 0.3125° to a maximum of 5° × 5° doubling at each step. The thresholds for the global meshing are 5000, 7000, 8000 and 9000 for coarsest mesh to finest mesh. The regional thresholds for North America (longitude 180° to 315°E and latitude 10° to 70°N and depth less than 1300 km) are 2000, 3000, 4000 and 5000 hits per voxel.

Figure S2. Trade-off curve for tested roughness damping at constant difference damping and norm damping. The red circle is our preferred value for SAVANI-US.

Figure S3. Effect of difference damping parameter on leakage. Most of the explored space is nearly linear and high difference damping values show a local maximum in isotropic variance.

Figure S4. Plot of power spectral density versus depth and spherical harmonic degree for isotropic velocity models compared in Figure 4. Higher spherical harmonic degree corresponds to shorter wavelength structures. SAVANI is by Auer *et al.* (2014), SAVANI-US our new model, S40RTS by Ritsema *et al.* (2011) and S362ANI-M by Moulik & Ekstrom (2014).

Figure S5. Models of radial anisotropy focused under the contiguous United States. Model names on top are the same as per the main paper. NASEM is by Clouzet *et al.* (2018).

Figure S6. Result of a resolution test with a thick craton in the upper 200 km and a 200 km thick slab in the transition zone. The input model is our best-fitting model but with the structure in the central United States replaced for the test (top panel). The output shows that the zone of neutral velocity anomaly separating the slab and the craton is poorly resolved and replaced with structure smeared between the slab and the craton.

Figure S7. Comparison of seismic tomography models along a profile similar to Fig. 7b (A–A′). Models along the top row are focused on the continuous United States and use body waves and surface waves in the case of SAVANI-US and MITS_BWSW. Models in the middle row are relatively smooth, global models. Models along the bottom row are *P* wave only models. MITS_BWSW is by Golos *et al.* (2018), TX2019 by Lu *et al.* (2019, version without prescribed slabs), SEMUCB-WM1 by French & Romanowicz (2014), GAP_P4 by Obayashi *et al.* (2013) and Fukao & Obayashi (2013) and UU-P07 by Amaru (2007) and Hall & Spakman (2015).

Figure S8. Comparison of velocity models along a profile similar to Fig. 7(c) (B–B′). See caption for S7 for model description.